# Wavelength-division-multiplexed and identical -weak Bragg grating arrays in multicore fiber for single-channel OFDR shape sensing

YANJIE MENG, 1,2,3 D RONGYI SHAN, 1,2 WENFA LIANG, 1,2 SHUAI XIAO,<sup>1,2</sup> HUAJIAN ZHONG,<sup>1,2</sup> YUHAO KONG,<sup>1,2</sup> ZHENWEI PENG,<sup>1,2</sup> WEIJIA BAO,<sup>1,2</sup> CAILING FU,<sup>1,2,\*</sup> YATAO YANG, 4 AND YIPING WANG 1,2

**Abstract:** The multicore fiber shape sensing technique faces challenges in system complexity and cost due to the need for simultaneous measurement of multiple cores, and the massive data volume increases computation time. In this work, we report a single-channel optical frequency domain reflectometry (OFDR) shape sensing method using wavelength-division-multiplexed (WDM) and identical-weak (IW) Bragg grating arrays in multicore fiber. The WDM grating arrays are multiplexed in seven cores and IW grating arrays are connected in series within each core. This method enables synchronous strain measurement of seven cores through a single scan and without extra optical device. In experiments, we fabricated 1.5mm-long gratings in all seven cores using femtosecond laser direct writing, achieving strain measurement accuracy below 6 µE with 1.5 mm spatial resolution. We also demonstrate fiber shape reconstruction at a length of 0.40 m, with the maximum shape reconstruction errors per unit length are 2.61% and 2.75% for 2D and 3D shape, respectively. Furthermore, we conducted a proof-of-concept experiment by integrating the shape-sensing fiber into a medical catheter and navigating through an arterial model, successfully reconstructing the catheter's 3D shape within the model and validate its potential for endovascular interventions.

© 2025 Optica Publishing Group under the terms of the Optica Open Access Publishing Agreement

#### Introduction

Fluoroscopically-guided endovascular interventions have emerged as a primary treatment modality for various vascular pathologies. However, a limitation of this approach is its reliance on twodimensional (2D) projection imaging, which fails to provide real-time three-dimensional (3D) visualization of devices within complex vascular anatomies [1,2]. This limitation prolongs procedure times and inadvertently increases patient's exposure to ionizing radiation [3]. To address these challenges, advanced imaging modalities such as computed tomography angiography (CTA) and magnetic resonance angiography (MRA) have been integrated with endovascular treatment [4]. While these techniques enhance anatomical 3D visualization, they do not improve the ability of device tracking in 3D space, leaving operators unable to fully comprehend the spatial relationship between devices and vasculature.

 $<sup>^{</sup>I}$ Shenzhen Key Laboratory of Photonic Devices and Sensing Systems for Internet of Things, Guangdong and Hong Kong Joint Research Centre for Optical Fibre Sensors, State Key Laboratory of Radio Frequency Heterogeneous Integration, Shenzhen University, Shenzhen 518060, China

<sup>&</sup>lt;sup>2</sup>Shenzhen Key Laboratory of Ultrafast Laser Micro/Nano Manufacturing, Key Laboratory of Optoelectronic Devices and Systems of Ministry of Education/Guangdong Province, College of Physics and Optoelectronic Engineering, Shenzhen University, Shenzhen 518060, China

<sup>&</sup>lt;sup>3</sup>Guangdong Laboratory of Artificial Intelligence and Digital Economy (SZ), Shenzhen 518107, China <sup>4</sup>College of Electronics and Information Engineering, Shenzhen University, Shenzhen 518060, China

<sup>\*</sup>fucailing@szu.edu.cn

Optical fiber shape sensing (OFSS) represents a promising solution to this problem [5–8]. As a contact-based 3D shape measurement technology, OFSS utilizes microscale optical fibers (comparable in size to a human hair) embedded within devices to enable real-time 3D shape tracking. Notably, optical fibers are immune to electromagnetic interference, making them ideally suited for medical applications. A first in human study [8] has demonstrated the feasibility of OFSS for real-time 3D device navigation in abdominal and peripheral endovascular procedures.

Distributed optical fiber sensing (DOFS) technologies, including Brillouin optical time-domain analyzer [9] and optical time-domain reflectometry [10], optical frequency domain reflectometry (OFDR) [11], as well as fiber Bragg grating (FBG) [12] [13], have been widely explored for shape sensing applications. Among these, multicore fiber Bragg grating (MCF-FBG) arrays combined with OFDR have emerged as a preferred solution for constructing high-performance OFSS [11,14]. This hybrid approach leverages distributed sensing capabilities and submillimeter-scale spatial resolution, enabling high-precision real-time 3D shape reconstruction.

Shape sensing using OFDR requires differential strain distributions of the cross sections along the fiber. Several methods have been developed to measure strain distribution of each individual core. The most common-used method is using an optical switch to scan each core in sequence [15,16]. The strain distribution then can be measured in different time slots. But information from each measure corresponds to different shape state of the fiber, which would reduce accuracy and unable achieve dynamic shape sensing. To achieve synchronous measurement, multiple main interferometers were adopted in an OFDR system, and use multi-channel detector module to enable simultaneous measurement per core [17,18], which would increase costs. Wing Ko et al. used a distal graded index (GRIN) fiber micro-turnaround to connect multiply cores in series with a single-channel OFDR, which also could enable the synchronization but increase the measurement length and introduce  $\sim$ 2 dB round-trip loss [19]. Recently, a single-channel OFDR shape sensing method was proposed to simultaneously measure strain distribution of three cores, only employs Rayleigh-signature domain and without extra optical device [20,21]. However, the increasing core counts degrade the measurement accuracy and spatial resolution.

Currently, shape sensing primarily employs two types of fiber grating arrays: identical-weak fiber Bragg grating (IW-FBG) arrays and wavelength-division multiplexing fiber Bragg grating (WDM-FBG) arrays, which can be fabricated using ultraviolet (UV) laser and femtosecond laser manufacture techniques [22–26]. Due to the fixed period of the phase mask, UV laser fabrication is generally limited to producing IW-FBG arrays. The preparation of WDM-FBG arrays is more complex, requiring the replacement of different phase masks and splicing them together [13]. On the other hand, femtosecond laser direct-writing techniques (e.g., point-by-point method) offers greater flexibility, enabling the straightforward fabrication of both types of grating arrays [12,14]. To date, IW-FBG arrays are combined with OFDR for shape sensing [14,22], while WDM-FBG arrays rely on FBG demodulation system for sensing measurements [12]. The broad frequency-sweeping capability of OFDR endows it with high spatial resolution. However, in shape sensing applications using IW-FBG arrays, only a portion of the spectral domain is utilized. To date, no studies have investigated the integration of OFDR with WDM-FBG arrays to fully exploit the entire spectral domain, which could further enhance sensing performance.

In this work, we propose what we believe to be a novel single-channel OFDR shape sensing method based on WDM- and IW- FBG arrays, where WDM grating arrays are multiplexed in seven cores and the same core integrate the IW grating arrays. This method enables synchronous high-precision strain measurement of all grating arrays in seven cores through a single measurement only using a main interferometer of the OFDR system while maintaining high spatial resolution. Utilizing this shape sensing technique, we successfully achieved both 2D and 3D shape reconstruction. Furthermore, we conducted a proof-of-concept experiment in an arterial model by integrating the optical fiber into a medical catheter and navigating through

an arterial model, which demonstrated successful 3D shape reconstruction of the catheter both outside the model and when inserted into the iliac and external iliac artery tunnels.

### 2. System setup and operation principle

The experimental setup for single-channel OFDR shape sensing based on WDM- and IW- FBG arrays in MCF was depicted in Fig. 1. The light from the tunable laser source (TLS) is split into two parts by a 10:90 optical coupler, entering the auxiliary interferometer (AI) and main interferometer (MI), respectively. The AI generates a beat-frequency signal for zero-crossing resampling, compensating phase noise induced by the nonlinear frequency sweep of the light source. Meanwhile, the MI serves as the primary sensing branch: its beam is equally divided by a  $1 \times 8$  optical splitter, with each output port connected to a fan-in/fan-out (FIFO) module to simultaneously inject light into all seven cores of the MCF. The reflected sensing signals from all FBGs are then routed back to the MI. Both AI and MI beat signals are detected by balanced photodetectors (BPDs), digitized via a data acquisition card (DAQ), and subsequently processed by a central processing unit (CPU) for demodulation and analysis.

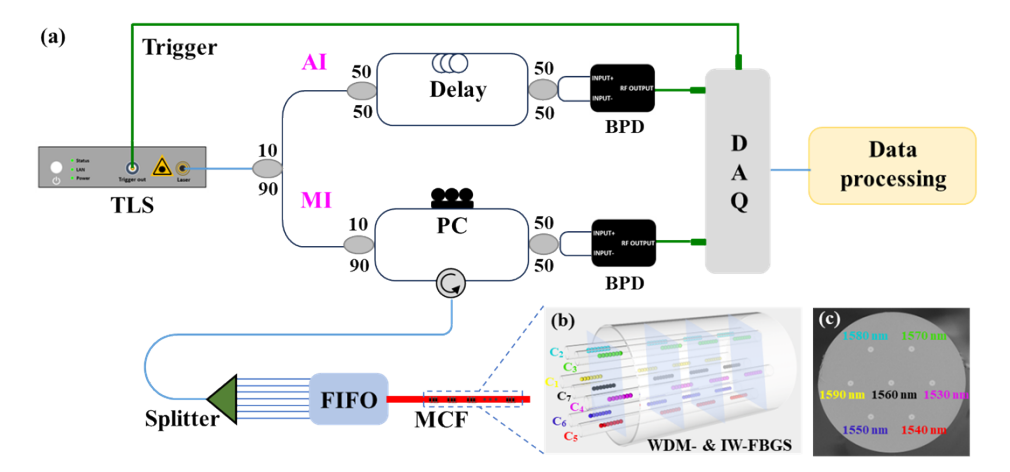


**Fig. 1.** (a) Experimental setup for single-channel OFDR shape sensing based on WDM-and IW- FBG arrays in MCF. AI: auxiliary interferometer; MI: main interferometer; TLS: tunable laser source; PC: polarization controller; BPD: balanced photodetector; DAQ: data acquisition card; FIFO: fan-in-fan-out. MCF: multicore fiber. (b) The longitudinal distribution of gratings along the MCF and (c) the central wavelength distribution within the same cross-section of different cores.

The employed MCF has seven cores as shown in Fig. 1(b): the six outer cores are distributed in a regular hexagon and one core is located at the center. The average distance between outer cores and the central core is 79.7  $\mu$ m. This relatively large core-to-core distance effectively minimizes the accumulation of shape reconstruction errors [27]. The fiber features a 250  $\mu$ m cladding diameter with an additional 1 mm protective coating, which provides inherent mechanical robustness against minor torsional stresses. It should be noted that complete compensation for torsional effects would require the implementation of helical multicore fiber [28]. The designed central wavelengths of the gratings in the seven fiber cores are 1590 nm (Core<sub>1</sub>, abbreviated as C<sub>1</sub>), 1580 nm (C<sub>2</sub>), 1570 nm (C<sub>3</sub>), 1560 nm (C<sub>7</sub>), 1550 nm (C<sub>6</sub>), 1540 nm (C<sub>5</sub>), and 1530 nm (C<sub>4</sub>), respectively, as shown in Fig. 1(c). This 10-nm wavelength spacing between adjacent cores ( $\Delta\lambda$  = 10 nm) creates non-overlapping spectral channels that enable unambiguous core identification. The TLS was linearly swept from 1520 nm to 1600 nm at a sweep rate of 200 nm/s to ensure complete coverage of all grating operational bandwidth.

The signal acquired by the MI represents a superposition of reflected signals from WDM-FBG arrays in each core. This superposition exhibits unique spatial-spectral characteristics: while WDM-FBG arrays at the same cross-sectional position overlap in the distance domain, those at different axial positions remain separable. On the other hand, gratings in different cores remain distinguishable in the wavelength domain due to their distinct center wavelengths, with each occupying a dedicated spectral bandwidth corresponding to its respective core. The calculation procedure of the single-channel OFDR shape sensing based on WDM- and IW- FBG arrays in MCF is shown in Fig. 2. Step 1: the compensated time-domain data from MI were transformed into distance domain by fast Fourier transform (FFT), which seven WDM-FBG arrays in same cross-section were superimposed at the same position. Step 2: the distance-domain data of this array was selected using a rectangular window, which then was zero-padding and transformed into the wavelength domain using inverse fast Fourier transform (IFFT), i.e., obtaining overall spectrum of this WDM-FBG array. Step 3: band segmentation isolates individual spectra based on the center wavelength of each FBG. Each specific spectra corresponds to a particular fiber core. Step 4: quadratic polynomial peak fit was used to obtain the center wavelength. With iterative repetition of steps 2-4, we can obtain center wavelength of all arrays. Step 5: the baseline measurement was performed while the fiber was in a straight configuration. The center wavelengths obtained from this baseline measurement were then subtracted from those recorded during shape sensing to determine the wavelength shifts. Then multiply these shifts by the strain coefficient to derive the strain values for each FBG array within individual fiber cores. Step 6: temperature/axial strain compensation is achieved by subtracting central core strain values from outer cores. Step 7: the apparent curvature vector (APP) method [11] computes local curvature and bending orientation from strain distribution of outer cores. Step 8: the 3D shape of the fiber is reconstructed through Bishop frame [21].

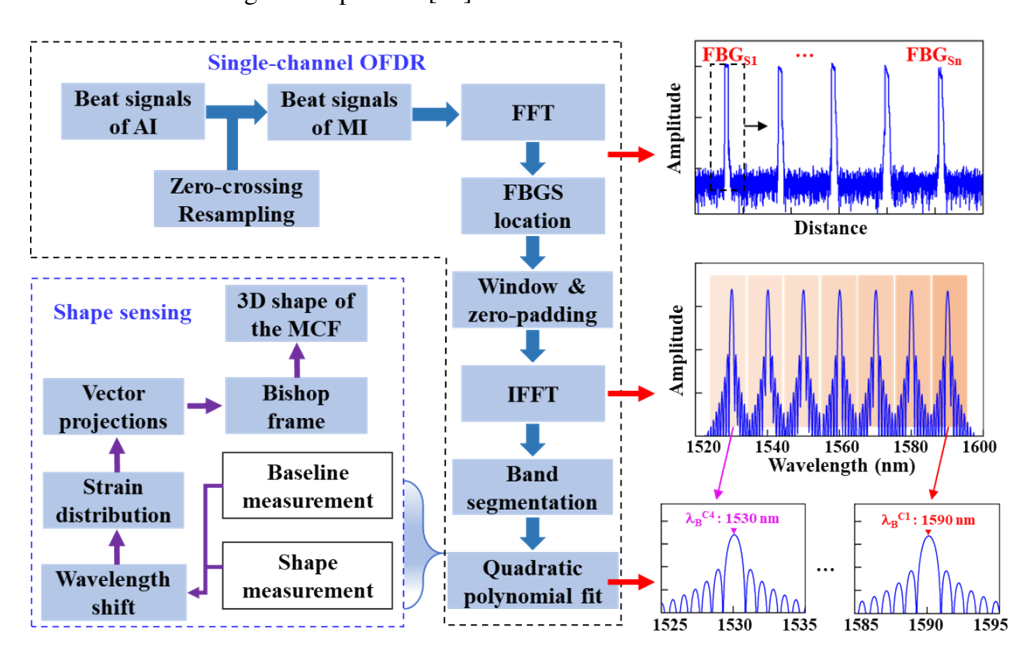


**Fig. 2.** Calculation procedure of the single-channel OFDR shape sensing based on WDM-and IW- FBG arrays in MCF. FFT: fast Fourier transformation; IFFT: inverse FFT.

## 3. Experimental results and discussion

The WDM- and IW- FBG arrays were inscribed in a MCF with a polymer coating layer using the femtosecond laser point-by-point (PbP) method as shown in Fig. 3(a). The detailed fabrication setup can be found in the Ref. [12]. The parameters of this grating array are as follows: each FBG had a length of 1.5 mm with 2 cm spacing between adjacent gratings within the same core, and 20 gratings were inscribed in each core. The total length of the WDM- and IW- FBG arrays for shape sensing was 40 cm. The single-channel OFDR system shown in Fig. 1 was employed for measurement. Figure 3(b) presents the distribution of the grating arrays in the distance domain, where gratings at the same position appear overlapped. The composite reflection spectrum of FBGs in all seven cores at the first grating array position is shown in Fig. 3(c), showing distinct Bragg peaks with central wavelengths at 1530.562, 1539.63, 1549.118, 1559.526, 1570.379, 1578.832, and 1588.926 nm, respectively. This wavelength distribution demonstrates successful fabrication of WDM-FBGs in different cores.

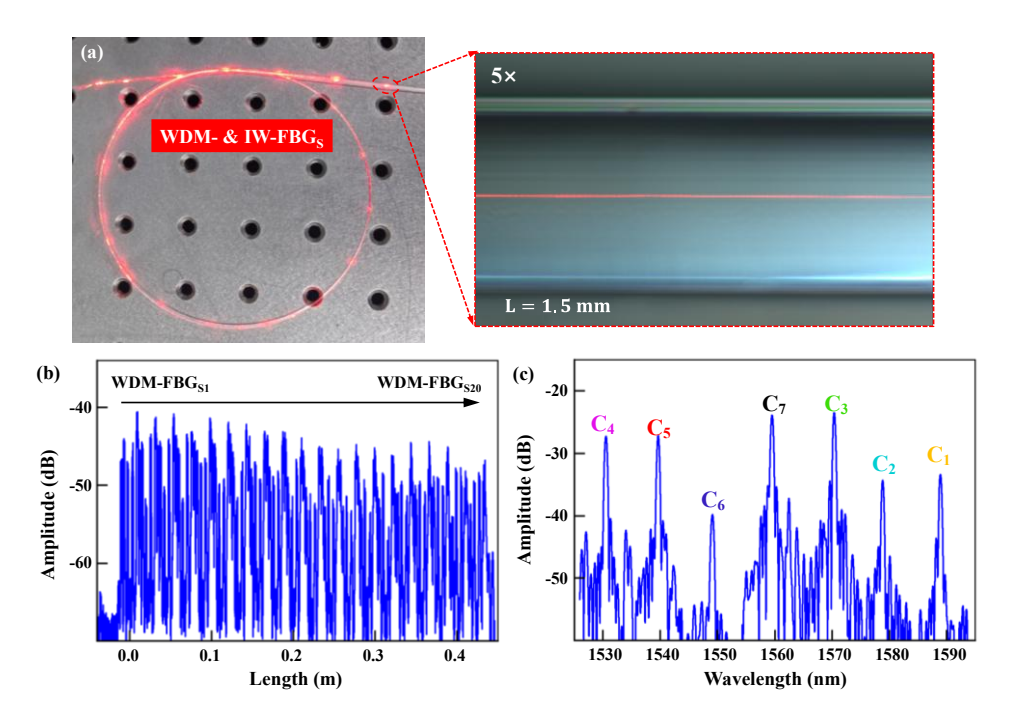


**Fig. 3.** (a) Fabricated WDM- and IW- FBG arrays in a seven-core fiber. Inset: optical micrograph of WDM-FBGs<sub>1</sub>. (b)The distribution of the WDM- and IW- FBG arrays along the fiber measured by the single-channel OFDR. (c) The composite spectrum of WDM-FBGs<sub>1</sub> demodulated using the calculation procedure shown in Fig. 2(b).

The bending characteristics of the WDM-FBGs then were investigated. It is worth mentioning that each spectrum was normalized following band segmentation to ensure consistent signal intensity for comparison of different cores. As shown in Fig. 4(a), when the fiber was bent, the central wavelength of the grating in the central core  $(C_7)$  remained unchanged. For gratings located on the outer side of the bent fiber  $(C_1, C_2, C_6)$ , tensile stress caused a redshift (long-wavelength shift), while those on the inner side  $(C_4, C_5, C_3)$  experienced compressive stress leading to a blueshift (short-wavelength shift). Notably, gratings positioned  $180^\circ$  apart exhibited wavelength shifts of similar magnitude but opposite directions.

To quantify the bending response, we measured the wavelength shifts under different bending curvature and orientation. Firstly, the MCF was embedded into semicircular grooves with radii

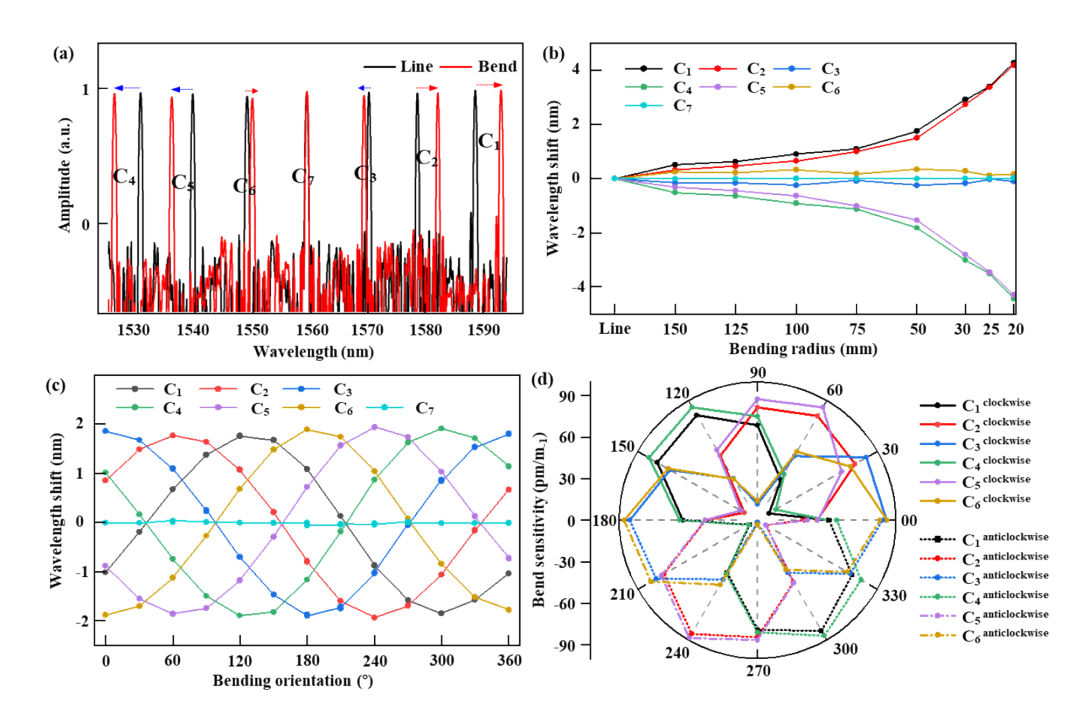


**Fig. 4.** (a) Wavelength shift characteristics of FBGs in seven cores under bending. (b) Wavelength shifts of six outer-core FBGs versus bending radius of 150, 125, 100, 75, 50, 30, 25, and 20 mm, respectively. (c) Wavelength shifts versus bending orientation from 0° to 360° at a fixed radius of 50 mm. (d) Polar plot of bending sensitivity for six outer-core WDM-FBGs.

of 150, 125, 100, 75, 50, 30, 25, and 20 mm, with five repeated measurements for each condition. As shown in Fig. 4(b), the absolute wavelength shift increased as the bending radius decreased. Given the 10 nm operational bandwidth of each FBG, the minimum detectable bending radius was determined to be 20 mm. Then, the fiber was bent at a fixed radius of 50 mm while being rotated in 60° increments from 0° to 360° using two rotary fiber holders. Five measurements were taken at each angle. As shown in Fig. 4(c), the wavelength shifts of each FBG followed a sinusoidal behavior, confirming the directional dependence of the bending response. The bending sensitivities of the six outer cores  $(C_1-C_6)$  were plotted in a polar coordinate system (Fig. 4(d)), forming six distinct 'figure-8' patterns. Each pattern exhibited two maxima and minima: the sensitivity reached its peak when the bending orientation is coincided with the axis connecting this FBG and fiber center, while it became minimal when orthogonal. We performed cosine curve fitting to determine the maximum wavelength shift. The maximum bending sensitivity was then calculated by dividing this maximum value by the applied curvature. The maximum bending sensitivities for the six gratings were calculated as 90.29, 92.63, 92.64, 96.24, 95.25, and 92.5 pm/m<sup>-1</sup>, respectively. It facilitates the estimation of operating bandwidth requirements for individual gratings based on application-specific curvature ranges. These results highlight the strong directional dependance between bending and wavelength shift, making the sensor suitable for shape reconstruction.

In addition, we evaluated the strain measurement accuracy by calculating the mean standard deviation from five repeated measurements across varying curvatures and bending orientations. The resulting strain accuracies for the WDM-FBGs were 4.12, 4.63, 9.27, 3.09, 4.23, 3.86, and 5.44  $\mu \epsilon$  while maintaining a 1.5 mm spatial resolution. These results validate that the proposed single-channel OFDR method based on WDM- and IW- FBG arrays achieves both high spatial

resolution and high-accuracy strain measurement, overcoming the traditional trade-off between these parameters.

We conducted 2D and 3D shape sensing experiments using the WDM- and IW- FBG arrays. The shape reconstruction was performed following the setup in Fig. 1 and the procedure in Fig. 2. During experiments, we intentionally avoided applying twist to minimize torque effects, based on our practical experimental experience. For 2D shape sensing, the fiber was wound around a circular disk with 6.15 cm radius. As shown in Fig. 5(a) and (b), the standard deviation (SD) of curvature radius is 0.22 cm and the error is 0.42 cm, while the SD of bending orientation is 1.3°. It should be noted that while the bending orientation remained continuous, an abrupt curvature change was observed in the last FBG. This phenomenon can be attributed to incomplete fixation of the fiber tip to the disk, resulting in an increased reconstructed curvature radius. The reconstructed circle shown in Fig. 5(c) demonstrates accurate 2D shape. For 3D shape sensing, the fiber was embedded in a left-handed helical groove on a cylindrical surface (designed pitch = 10.3 cm, radius = 4.55 cm, theoretical torsion = 7.01 m<sup>-1</sup>). As shown in Fig. 5(d) and (e), the SD of curvature radius is 0.30 cm and the error is 0.42 cm, while the measured torsion of 7.019 m<sup>-1</sup>. The reconstructed helix shown in Fig. 5(f) demonstrates accurate 3D shape. The reconstruction errors per unit length were 2.61% for 2D and 2.75% for 3D shape sensing, based on the Euclidean distance deviation of the end-point position, confirming the capability of the proposed method for precise three-dimensional shape reconstruction.

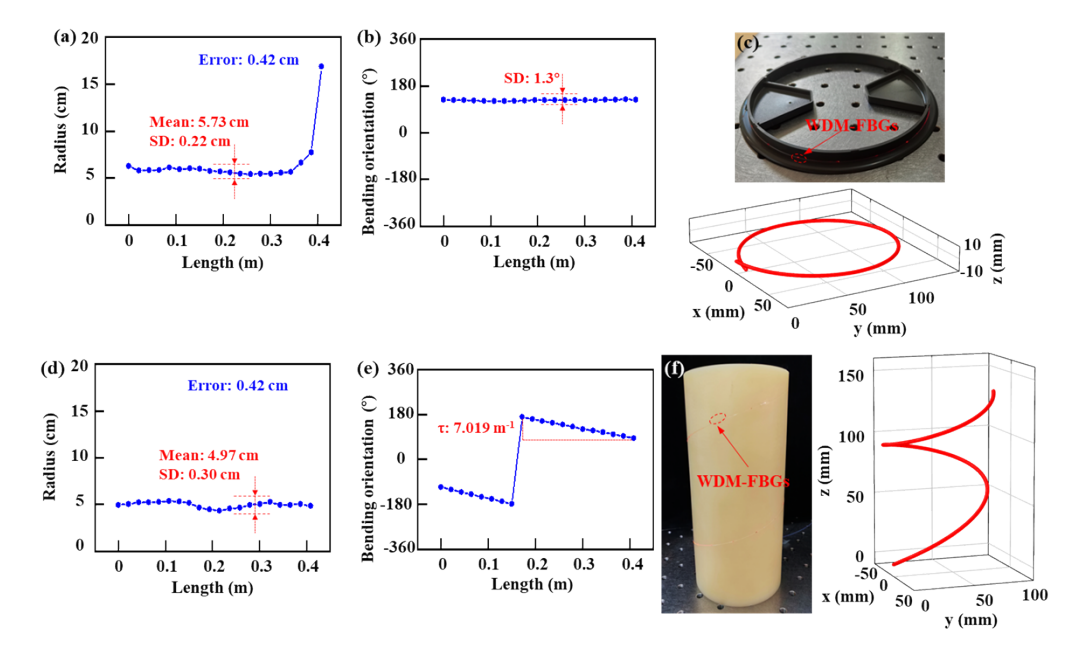


**Fig. 5.** Calculated (a) curvature radius, (b) bending orientation and (c) reconstructed fiber shape of a circular disk. Calculated (d) curvature radius, (e) bending orientation and (f) reconstructed fiber shape of a left-handed helical groove on a cylindrical surface.

To quantified the advantages of proposed method over multi-channel technique, we implemented a four-channel shape sensing system as shown in Fig. 6. Using identical laser parameters, we employed this method to repeatedly measure both 2D and 3D shapes. A comprehensive comparison between the multi-channel technique and our proposed method is presented in Table 1. Experimental results demonstrated that our proposed method delivers three key advantages: a 40% reduction in data volume, a 70% improvement in computation time, and maintained strain acquisition synchronization, all while limiting shape sensing precision degradation to no more

than 0.10%. From a cost perspective, our approach demonstrates substantial savings: a 2-channel DAQ configuration reduces hardware costs by approximately 66% compared to a multi-channel system, while femtosecond laser fabrication maintains equivalent expenses for FBG arrays. The proposed method enables synchronous, high-spatial-resolution and high-precision strain measurements across all seven fiber cores without requiring additional hardware systems or introducing computational burdens from massive data volumes.

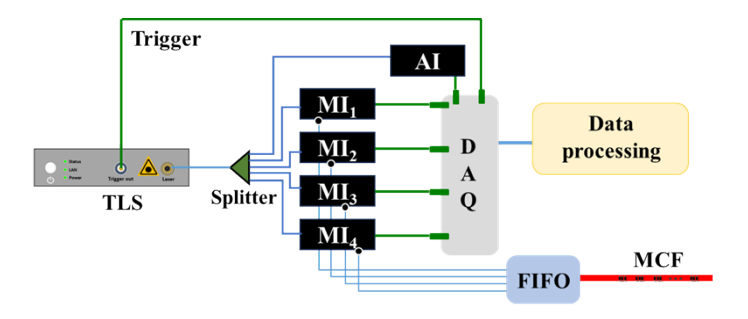
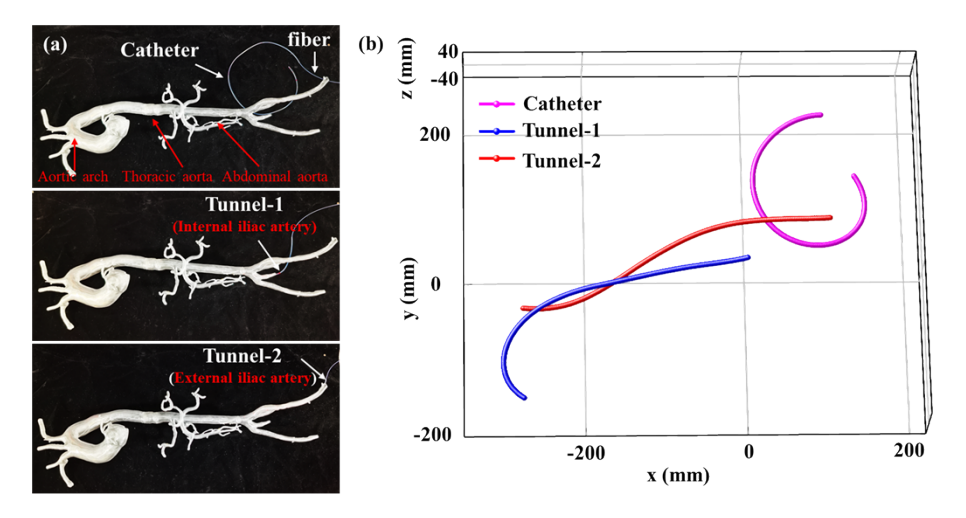


Fig. 6. Experimental setup for multi-channel OFDR shape sensing.

Table 1. Comparison between the proposed technique and multi-channel technique

	Data volume (MB)	Computation time (s)	System cost	Relative accuracy (2D)	Relative accuracy (3D)
Multi-channel technique	192	67.65	Increase	2.51%	2.68%
Proposed technique	76.8	20.66	Non- increase	2.61%	2.75%



**Fig. 7.** (a) The combined catheter-fiber structure advanced through an arterial model's internal iliac artery (Tunnel-1) and external iliac artery (Tunnel-2). (b) Reconstructed 3D shape of the catheter within the arterial model.

To validate the potential application of the proposed method for endovascular interventions, we conducted a proof-of-concept experiment using an arterial model. As shown in Fig. 7(a),

the experimental procedure involved: (1) inserting the optical fiber into a medical catheter which can provide additional torsion isolation [13]. (2) advancing the combined catheter-fiber structure sequentially through the model's internal iliac artery (Tunnel-1) and external iliac artery (Tunnel-2). As shown in Fig. 7(b), the catheter's 3D shape within the arterial model were reconstructed using our proposed sensing method. When navigating from the Tunnel-1 through the abdominal aorta, thoracic aorta, and aortic arch, the complete anatomical course with all curvatures and bifurcations was successfully reconstructed. Similarly, the partial pathway from the Tunnel-2 through the abdominal aorta to the thoracic aorta was also correctly reconstructed. This proof-of-concept experiment suggests potent ion of the proposed method to track complex 3D vascular paths.

#### 4. Conclusion

In conclusion, this study demonstrates a novel single-channel OFDR shape sensing technique based on WDM- and IW- FBG arrays in MCF. Experimental results validated the system's capability for both 2D and 3D shape reconstruction, as evidenced by the proof-of-concept experiment in an arterial model. The proposed method enables synchronous, high-spatial-resolution and high-precision strain measurements across all seven fiber cores without requiring additional hardware systems or introducing computational burdens from massive data volumes. This approach can be directly implemented on the existing single-channel OFDR systems for shape sensing applications. Future developments will focus on two key improvements: (1) system optimization for real-time operation through FPGA or GPU acceleration to enhance computational efficiency, (2) further miniaturization for in vivo applications by integrating couplers directly within the MCF to eliminate beam splitters and fan-in/fan-out devices, creating a more compact plug-and-play shape sensing fiber system. These advancements hold particular promise for medical applications requiring both high-speed processing and compact form factors.

**Funding.** National Key Research and Development Program of China (2023YFB3209500); National Natural Science Foundation of China (U22A2088, 62375178, 62222510, 62405196); Shenzhen Science and Technology Program (JCYJ20220818095800001, JCYJ20241202124226032); LingChuang Research Project of China National Nuclear Corporation (CNNC-LCKY-202265); China Postdoctoral Science Foundation (2024M752106, GZC20231715).

**Disclosures.** The authors declare no conflicts of interest.

**Data Availability.** Data underlying the results explained in this paper are not publicly available at this time but may be obtained from the authors upon reasonable request.

#### References

- Y. G. Wolf, M. Tillich, W. A. Lee, et al., "Impact of aortoiliac tortuosity on endovascular repair of abdominal aortic aneurysms: Evaluation of 3D computer-based assessment," J. Vasco. Surg. 34(4), 594–599 (2001).
- K. M. Brazil, R. Chasan, E. Kahuku, et al., "Transcatheter aortic valve implantation: our experience and review of the literature," Balkan Med. J. 29(2), 118–123 (2012).
- A. S. Thakor, A. Winterbottom, M. Mercuri, et al., "The radiation burden from increasingly complex endovascular aortic aneurysm repair," Insights into Imaging 2(6), 699–704 (2011).
- N. Abi-Joudah, H. Ko Beiter, and S. Xu, "Image fusion during vascular and nonvascular image-guided procedures," Techniques Vascular Intervent. Radiol. 16(3), 168–176 (2013).
- 5. T. M. Bayldon, A. Torgersen, S. Pokeroot, *et al.*, "3D visualization of navigation catheters for endovascular procedures using a 3D hub and fiber optic Real Shape technology: Phantom Study Results," Eves Vasc. Forum. **59**, 24–30 (2023).
- A. Svecic, J. Francoeur, G. Soulez, et al., "Shape and flow sensing in arterial image guidance from UV exposed optical fibers based on spatio-temporal networks," IEEE Trans. Biomed. Eng. 70(5), 1692–1703 (2023).
- J. Francoeur, D. Lezcano, Y. Zhetpissov, et al., "Fully distributed shape sensing of a flexible surgical needle using optical frequency domain reflectometry for prostate interventions," IEEE Internat. Conf. Robotics Automat. 2024, 17594–17601 (2024).
- 8. J. A. van Herwaarden, M. M. Jansen, E. J. P. A. Vonken, *et al.*, "First in human clinical feasibility study of endovascular navigation with fiber optic RealShape (FORS) technology," Eur. J. Vasc. Endovasc. **61**(2), 317–325 (2021).
- Z. Y. Zhao, M. A. Soto, M. Tang, et al., "Distributed shape sensing using Brillouin scattering in multi-core fibers," Opt. Express 24(22), 25211–25223 (2016).
- L. Szostkiewicz, M. A. Soto, Z. S. Yang, et al., "High-resolution distributed shape sensing using phase-sensitive optical time-domain reflectometry and multicore fibers," Opt. Express 27(15), 20763–20773 (2019).

- J. P. Moore and M. D. Rogge, "Shape sensing using multi-core fiber optic cable and parametric curve solutions," Opt. Express 20(3), 2967–2973 (2012).
- 12. Y. J. Meng, S. Xiao, R. Y. Shan, *et al.*, "Length-extended 3D shape sensor using wavelength/space-division multiplexing grating arrays in a multicore fiber," Opt. Lett. **49**(15), 4146–4149 (2024).
- 13. L. X. Meng, H. Xu, and Y. Y. Huang, "High-accuracy 3D shape sensor based on anti-twist packaged high uniform multicore fiber FBGs," Adv. Fiber Mater. 5(4), 1467–1477 (2023).
- C. Fu, S. Xiao, Y. Meng, et al., "OFDR shape sensor based on a femtosecond-laser-inscribed weak fiber Bragg grating array in a multicore fiber," Opt. Lett. 49(5), 1273–1276 (2024).
- Y. J. Meng, C. L. Fu, C. Du, et al., "Shape sensing using two outer cores of multicore fiber and optical frequency domain reflectometer," J. Lightwave Technol. 39(20), 6624–6630 (2021).
- C. Fu, Y. Meng, L. Chen, et al., "High-spatial-resolution φ-OFDR shape sensor based on multicore optical fiber with femtosecond-laser-induced permanent scatter arrays," Opt. Lett. 48(12), 3219–3222 (2023).
- 17. Z. Chen, C. H. Wang, Z. Y. Ding, *et al.*, "Demonstration of large curvature radius shape sensing using optical frequency domain reflectometry in multi-core fibers," IEEE Photonics J. **13**(4), 1–9 (2021).
- S. Li, Q. R. Li, Z. Y. Ding, et al., "Twist compensated, high accuracy and dynamic fiber optic shape sensing based on phase demodulation in optical frequency domain reflectometry," Mech. Syst. Signal Pr. 216, 111462 (2024).
- 19. W. Ko, K. S. Feder, X. G. Sun, *et al.*, "Simultaneous interrogation of multiple cores in a shape sensor fiber with a graded index fiber micro-turnaround," Opt. Express **30**(14), 24452–24460 (2022).
- M. Cappelletti, A. Aitkulov, D. Orsuti, et al., "Distributed fiber optic shape sensing with simultaneous interrogation of multiple fibers based on Rayleigh-signature domain multiplexing," Opt. Lett. 48(22), 5907–5910 (2023).
- Y. Meng, R. Sui, W. Liang, et al., "Multicore fiber shape sensing based on optical frequency domain reflectometry parallel measurements," J. Lightwave Technol. 42(10), 3909–3917 (2024).
- P. S. Westbrook, T. Kremp, K. S. Feder, et al., "Continuous multicore optical fiber grating arrays for distributed sensing applications," J. Lightwave Technol. 35(6), 1248–1252 (2017).
- A. Donko, M. Beresna, Y. Jung, et al., "Point-by-point femtosecond laser micro-processing of independent core-specific fiber Bragg gratings in a multi-core fiber," Opt. Express 26(2), 2039–2044 (2018).
- M. X. Hou, K. M. Yang, J. He, et al., "Two-dimensional vector bending sensor based on seven-core fiber Bragg gratings," Opt. Express 26(18), 23770–23781 (2018).
- A. Wolf, A. Dostovalov, K. Bronnikov, et al., "Arrays of fiber Bragg gratings selectively inscribed in different cores of 7-core spun optical fiber by IR femtosecond laser pulses," Opt. Express 27(10), 13978–13990 (2019).
- 26. X. Z. Xiao, B. J. Xu, X. Z. Xu, et al., "Femtosecond laser auto-positioning direct writing of a multicore fiber Bragg grating array for shape sensing," Opt. Lett. 47(4), 758–761 (2022).
- 27. S. Li, P. D. Hua, Z. Y. Ding, *et al.*, "Reconstruction error model of distributed shape sensing based on the reentered frame in OFDR," Opt. Express **30**(24), 43255–43270 (2022).
- 28. K. Y. Yang, C. J. Ke, Z. K. Xv, et al., "High accuracy calibration method for 3D curve reconstruction based on a twisted multicore fiber," Opt. Lett. **50**(6), 2113–2116 (2025).